Designed Bithiophene-Based Interfacial Layer for High-Efficiency Bulk-Heterojunction Organic Photovoltaic Cells. Importance of Interfacial Energy Level Matching

ARTICLE *in* ACS APPLIED MATERIALS & INTERFACES · JANUARY 2010

Impact Factor: 6.72 · DOI: 10.1021/am900634a · Source: PubMed

6 AUTHORS, INCLUDING:

Alexander W. Hains
MicroLink Devices, Inc.
15 PUBLICATIONS **1,595** CITATIONS
SEE PROFILE

Charusheela Ramanan
VU University Amsterdam
10 PUBLICATIONS **294** CITATIONS
SEE PROFILE

Designed Bithiophene-Based Interfacial Layer for High-Efficiency Bulk-Heterojunction Organic Photovoltaic Cells. Importance of Interfacial Energy Level Matching

Alexander W. Hains, Charusheela Ramanan, Michael D. Irwin, Jun Liu, Michael R. Wasielewski,* and Tobin J. Marks*

Department of Chemistry, Argonne−Northwestern Solar Energy Research (ANSER) Center and Materials Research Center, Northwestern University, 2145 Sheridan Road, Evanston, Illinois 60208-3113

ABSTRACT This contribution describes the design, synthesis, characterization, and organic photovoltaic (OPV) device implementation of a novel interfacial layer (IFL) for insertion between the anode and active layer of poly(3-hexylthiophene) (P3HT):[6,6]-phenyl-C_{61}-butyric acid methyl ester (PCBM) bulk-heterojunction solar cells. The IFL precursor, 5,5′-bis[(*p*-trichlorosilylpropylphenyl)phenylamino]-2,2′-bithiophene ($PABTSi_2$), covalently anchors to the Sn-doped In_2O_3 (ITO) surface via the $-SiCl_3$ groups and incorporates a bithiophene unit to align the highest occupied molecular orbital (HOMO) energy with that of P3HT (5.0 eV). The synthesis and subsequent electrochemical analysis of $PABTSi_2$ indicates a HOMO energy of 4.9 eV, while the lowest uoccupied molecular orbital level remains sufficiently high, at 2.2 eV, to effectively block electron leakage to the OPV ITO anode. For the P3HT:PCBM OPV fabrication, $PABTSi_2$ is used as a spin-coated cross-linked (via $-SiCl_3$ hydrolysis and condensation) 1:2 blend with poly[9,9-dioctylfluorene-*co*-*N*-[4-(3-methylpropyl)]-diphenylamine] (TFB). Such devices exhibit an average power conversion efficiency of 3.14%, a fill factor of 62.7%, an open-circuit voltage of 0.54 V, and a short-circuit current of 9.31 mA/cm^2, parameters rivaling those of optimized PEDOT:PSS-based devices.

KEYWORDS: organic photovoltaics • interface • electron blocking

I. INTRODUCTION

Organic photovoltaic (OPV) cells have been the subject of intense research in the past several years (1−9). This interest reflects the many potential attractions that OPVs offer for solar power conversion, such as the use of low-cost, lightweight plastic materials; compatibility with flexible substrates; and adaptability to inexpensive, low-temperature, large-area, solution-based processing techniques, including spin coating and doctor blading, as well as roll-to-roll and inkjet printing. Since the pioneering vapor-deposited donor/acceptor (D/A) bilayer devices reported by Tang in 1986, having power conversion efficiencies (η_p) of 1% (10), the physical/mechanistic understanding of OPV function and reported power conversion efficiencies have progressed dramatically. In 1995, the first bulk-heterojunction (BHJ) OPVs were reported (11−13). This cell architecture increases the fraction of photogenerated excitons able to separate into free holes and electrons by significantly reducing the required mean exciton diffusion length, which is accomplished by creating numerous phase-separated D/A interfaces throughout the active layer rather than relying on a single interface. The BHJ cell design has been widely adopted and used with numerous active-layer materials to increase OPV efficiency (1, 3, 4). Notably, cells employing poly(phenylene vinylene)s or polythiophenes as electron donors and soluble fullerenes as electron acceptors have been extensively studied. Poly[2-methoxy-5-(3′,7′-dimethyloctyloxy)-1,4-phenylene vinylene] (MDMO-PPV):[6,6]-phenyl-C_{61}-butyric acid methyl ester (PCBM) cells have achieved efficiencies as high as ∼2.5% (14, 15), while poly(3-hexylthiophene) (P3HT):PCBM OPV efficiencies are even higher, with several groups reporting ∼5% (chemical structures shown in Figure 1) (16−19). If OPV power conversion efficiencies can be brought to 10%, as various studies have argued appears well within reach (20−23), "plastic" solar cells could become commercially viable (24).

An important consideration in advancing OPV understanding and ultimate efficiency is optimizing the interactions between the various functional BHJ layers. Improved understanding of OPV interfacial interactions should provide insight into processes that limit current η_p values to well below theoretical photon-to-electricity conversion efficiencies. These processes include electron−hole recombination (9, 25−30), charge leakage due to imperfect diodes (15, 18, 25, 31, 32), inefficient exciton scission (26, 33−35), and surface energy mismatches that lead to interfacial dewetting/delamination (36−40). The importance of such interfacial phenomena has been previously demonstrated in other optoelectronic devices such as organic light-emitting diodes (OLEDs). In OLEDs, for example, insertion of a hole transport/electron-blocking layer (HTL/EBL) between the hole-injecting

* E-mail: m-wasielewski@northwestern.edu (M.R.W.), t-marks@northwestern.edu (T.J.M.).

Received for review September 17, 2009 and accepted November 17, 2009

DOI: 10.1021/am900634a

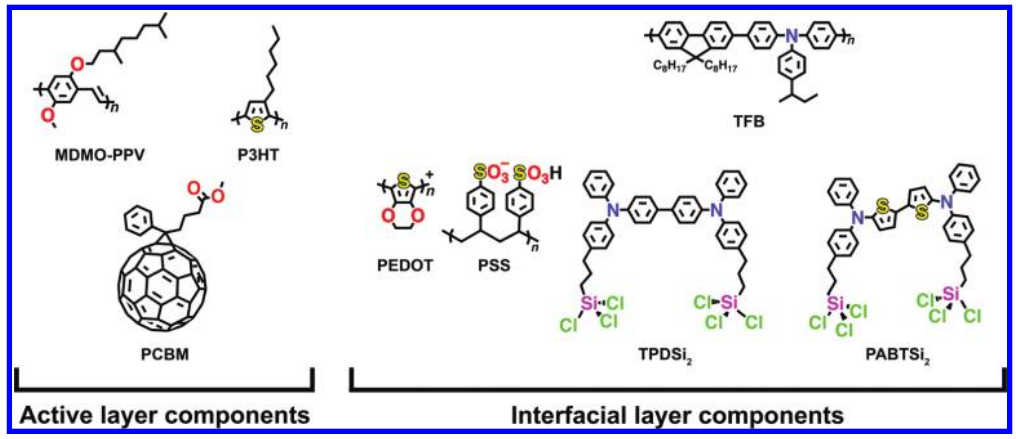

FIGURE 1. Structures and abbreviations of active-layer and IFL components used in this study.

Scheme 1. Depiction of (a) $TPDSi_2$ Covalent Bonding to the Hydroxylated ITO Surface and (b) Cross-Linking

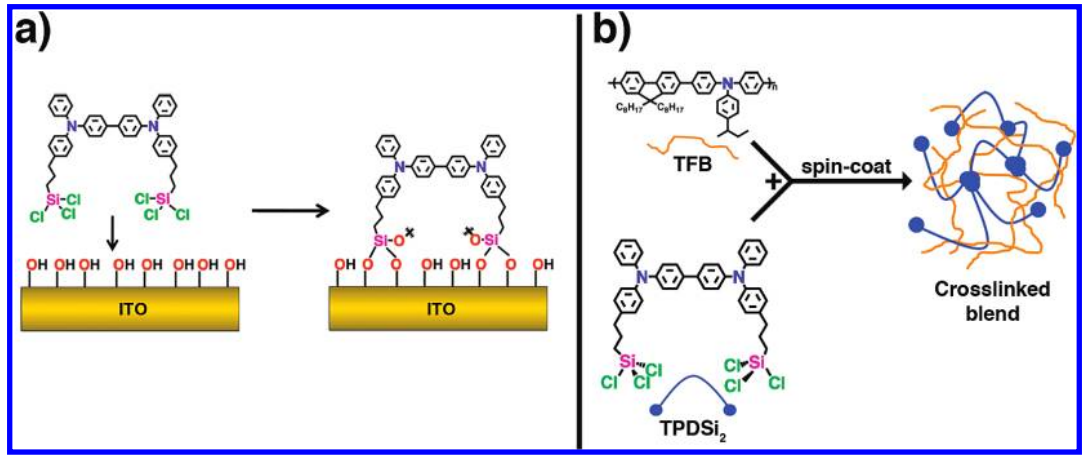

transparent conducting oxide (TCO) anode and the organic emissive layer (EML) both promotes hole injection and prevents injected electrons from transiting without radiative recombination, confining them to the EML for radiative recombination, which significantly increases the device efficiency (41−44).

In BHJ OPVs, interfacial layers (IFLs) have been used at both the cathode and anode sides of the active layer (15, 18, 25, 45−53). A thin LiF layer is typically deposited before the Al cathode (54, 55), a practice that will be employed consistently in this work, and poly(3,4-ethylenedioxythiophene):poly(styrene sulfonate) (PEDOT:PSS; Figure 1) is usually applied directly to the TCO anode, typically Sn-doped In_2O_3 (ITO), prior to active-layer deposition (4). The benefits of IFLs such as PEDOT:PSS in OPVs include creation of an ohmic contact (56), planarization of ITO surface "spikes" (57−59), increased open-circuit voltage (V_{oc}) (25, 57), and improved hole collection (60). PEDOT:PSS drawbacks include large electrical and microstructural inhomogeneities, which lead to widely varying conductivities and morphologies across the film surface, anisotropic conductivity that can lead to cross-talk between adjacent devices on a substrate, and pH ∼1, which can corrode the underlying ITO (2, 42, 61−65). Furthermore, PEDOT:PSS acidity effects are exacerbated at the high temperatures (66) inherent to most OPV operation, making PEDOT:PSS a nonoptimum IFL. In principle, many of these deficiencies should be addressable by using a more suitable IFL.

Recently, an IFL consisting of a cross-linked blend of 4,4′-bis[(*p*-trichlorosilylpropylphenyl)phenylamino]biphenyl ($TPDSi_2$) and poly[9,9-dioctylfluorene-*co*-*N*-[4-(3-methylpropyl)]diphenylamine] (TFB; Figure 1) was implemented in MDMO-PPV:PCBM OPVs, both in conjunction with and as a replacement for PEDOT:PSS (15, 25). This IFL functions as an HTL/EBL, which allows the collection of photogenerated holes at the anode but suppresses undesired electron leakage/recombination at the anode. Compared to PEDOT:PSS, this IFL displays superior charge-blocking characteristics, excellent thermal stability, and better electrode adhesion because of covalent bonding to the ITO surface (Scheme 1), while maintaining high hole mobility (field-effect transistor $\mu_h = 5 \times 10^{-4}$ cm^2/V · s), good optical transparency throughout the visible region of the spectrum, and insolubility in organic solvents, which allows subsequent active-layer deposition from solution.

While $TPDSi_2$ substantially increases MDMO-PPV:PCBM OPV V_{oc} and η_p metrics versus cells with no IFL or those with a PEDOT:PSS IFL, it curiously does not achieve similar enhancements for higher-performing P3HT:PCBM BHJ OPVs. Does this reflect an energy level mismatch between the $TPDSi_2$ and P3HT highest occupied molecular orbital (HOMO) energies, as shown in Figure 2? If this picture is valid, a

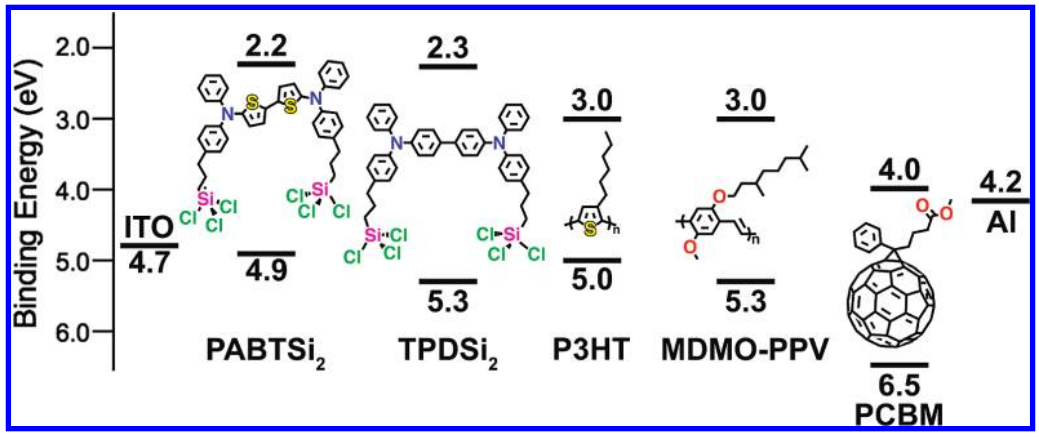

FIGURE 2. Energy level diagram depicting HOMO and LUMO energies of OPV device component materials, including that of the new IFL reported in this study, $PABTSi_2$.

P3HT:PCBM-compatible IFL would require a cross-linkable p-type semiconductor having substantial hole mobility, excellent chemical and thermal stability, good optical transparency, a high-lying lowest unoccupied molecular orbital (LUMO) to block misdirected electrons, and, importantly, a HOMO energetically positioned at or slightly above the P3HT HOMO to ensure facile hole extraction.

This contribution describes the design, synthesis, characterization, and BHJ OPV implementation of such an IFL, 5,5′-bis[(*p*-trichlorosilylpropylphenyl)phenylamino]-2,2′-bithiophene ($PABTSi_2$; Figure 2). It will be seen here that a thin layer of a $PABTSi_2$:TFB blend applied to the OPV anode is effective in producing P3HT:PCBM solar cell power conversion efficiencies rivaling those of analogous PEDOT:PSS-based cells.

II. EXPERIMENTAL SECTION

Materials and Methods. Anhydrous toluene, hexanes, and pentane for syntheses were purchased from Aldrich in PurePac containers and passed through a Grubbs column system (67) to further remove water and oxygen. TFB and $TPDSi_2$ were synthesized and purified according to the procedures of Yan et al. (42) and Huang et al. (43), respectively. PCBM was purchased from American Dye Source, Inc. It was purified by several cycles of sonication in toluene, followed by centrifugation, and then sonication in pentane, followed by centrifugation. MDMO-PPV was synthesized according to the procedure of Mozer et al. (68) and was purified by repeated precipitation from methanol. P3HT was purchased from Rieke Metals, Inc., and was purified by sequential Soxhlet extractions with methanol and hexanes. Anhydrous chlorobenzene (CB) and anhydrous *o*-dichlorobenzene (ODCB) were purchased from Aldrich and were distilled from P_2O_5. PEDOT:PSS (1:6 by weight) was purchased from H. C. Starck under the name Baytron P VP AI 4083, stored in the dark at 4 °C, and used as received. Aluminum slugs (99.999%) were purchased from Sigma-Aldrich, LiF (99.98%) was purchased from Acros, and both were used as received. ITO-coated glass substrates [10.5 Ω/□; root-mean-square (rms) roughness = 1.60−2.34 nm] were purchased from Delta Technologies Ltd. in 25 × 75 mm strips. The UV-curable epoxy ELC-2500 used for device encapsulation was purchased from Electrolite Corp. All other materials were used as received unless otherwise specified. NMR spectra were recorded on Varian 500 MHz instruments. High-resolution mass spectrometry (HRMS) was performed using a ThermoFinnigan MAT 900 XL mass spectrometer. Elemental analyses were performed by Midwest Microlabs, LLC. Optical absorption spectra were obtained with Varian Cary 5000 UV−vis−near-IR spectrophotometer. Cyclic voltammetry (CV) measurements were carried out at a scan rate of 100 mV/s with a platinum working electrode in acetonitrile with 0.1 M tetrabutylammonium hexafluorophosphate ($Bu_4N^+PF_6^-$) as the electrolyte. A platinum counter electrode and a silver pseudoreference electrode were used with the ferrocene/ferrocenium (Fc/Fc^+) redox couple as the internal standard. The electrochemical potentials obtained with reference to the silver electrode were converted to the standard calomel electrode (SCE) scale using $E^{\circ}_{Fc/Fc^+} = 0.424$ V vs SCE (69, 70), and the oxidation potentials measured were converted to HOMO energies using the standard relationship ionization potential (IP) = $E^{ox}_{onset} + 4.4$ eV (71−73). Film thicknesses were measured with a stylus-based Tencor P10 surface profiler. At least two scans per film location were averaged to obtain thicknesses, and at least two locations on the film were tested to ensure reproducibility of the results. A JEOL JSPM-5200 atomic force microscope was used to characterize film morphologies via atomic force microscopy (AFM). Images were recorded using the tapping mode under ambient conditions with Applied NanoStructures ACTA Si cantilevers having n^+-Si tetrahedral tips with a 5−6 nm radius of curvature. Several locations of the film were examined to ensure reproducibility, and the rms roughness scans are reported over 4.5 × 4.5 μm or 9 × 9 μm areas. Current density−voltage (*J*−*V*) plots of solar cells were obtained using a Spectra Nova Technologies class A solar cell analyzer with a Xe lamp that simulates AM1.5G light from 400−1000 nm at 1000 W/m^2. Four-point contacts were made to test devices, and all tests were carried out under ambient conditions at 25 °C. Devices were masked before testing to ensure no additional current was obtained from outside the designated solar cell area being examined. The analyzer was calibrated using a Si solar cell fitted with a KG3 filter that was tested and certified by the National Renewable Energy Laboratory (NREL). The KG3 filter accounts for differences in the spectral response of silicon and organic polymers, and it ensures that the spectral mismatch correction factor approaches unity (74).

Synthesis of 1-Allyl-4-bromobenzene (1). In a Stille coupling reaction, 1-bromo-4-iodobenzene and allyltri-*n*-butyltin were reacted to yield **1**. Thus, tetrakis(triphenylphosphine)palladium(0) (1.976 g, 1.710 × 10^{-3} mol) was weighed out in a nitrogen-filled glovebox and transferred to a Schlenk line. Allyltri-*n*-butyltin (10.60 mL, 3.419 × 10^{-2} mol) and 1-bromo-4-iodobenzene (9.680 g, 3.422 × 10^{-2} mol) were added along with 115 mL of distilled, degassed 1,4-dioxane to yield a yellow reaction mixture that darkened to orange as the reaction progressed. The reaction mixture was stirred at 70 °C for 46 h until analysis by thin-layer chromatography (TLC; hexanes), and gas chromatography/mass spectrometry (GC/MS) showed that

the reaction was complete. The mixture was next cooled to room temperature and filtered through Celite (rinsing with hexanes), and the resulting solution was washed with both hexanes and water to remove PPh_3. Then the organic portion was dried over $MgSO_4$. Filtration through Celite and removal of the solvent in a rotary evaporator at <75 °C yielded an orange oil. Column chromatography on silica gel with hexanes as the eluant afforded only **1** and tri-*n*-butyltin iodide. These were separated via vacuum distillation at 160 mTorr, where **1** distills at ~50 °C (never exceed 75 °C, which can potentially cause allyl group isomerization) as a clear colorless oil (2.810 g, 42% yield). GC/MS: single peak (rel intens) *m/z* 198 (M^+, 46), 196 (M^+, 46), 117 (100), 115 (86). ^{1}H NMR ($CDCl_3$): δ 7.41 (d, $J = 8.5$ Hz, 2H), 7.07 (d, $J = 8.0$ Hz, 2H), 5.90 (m, 1H), 5.09 (m, 2H), 3.36 (d, $J = 7.0$ Hz, 2H).

Synthesis of *N*-(4-Allylphenyl)phenylamine (2). Tris(dibenzylideneacetone)dipalladium(0) [$Pd_2(dba)_3$; 0.2623 g, 2.864×10^{-4} mol] and tri-*tert*-butylphosphine (0.11 g, 5.437×10^{-4} mol) were weighed out in a glovebox, transferred to a Schlenk line, and stirred for ~5 min in hexanes before the addition of sodium *tert*-butoxide (2.000 g, 2.081×10^{-2} mol) as a slurry in hexanes, **1** (2.810 g, 1.426×10^{-2} mol), and 80 mL of hexanes. Next, distilled aniline (1.43 mL, 1.57×10^{-2} mol) was added over a period of ~3 min with stirring. A brown precipitate formed after ~5 min at room temperature, and stirring was halted after 2 h. The mixture was then filtered through Celite, and the hexanes were removed in vacuo at ≤45 °C so as to minimize allyl group isomerization. The resulting oil was then placed in a freezer at −23 °C for 1 h to solidify. The resulting solid was then recrystallized from pentane to yield light tan crystals of **2** (2.43 g, 82% yield), which were collected by filtration and rinsed three times with cold pentane. GC/MS: single peak (rel intens) *m/z* 210 ($M^+ + H$, 17), 209 (M^+, 100), 208 ($M^+ - H$, 29), 182 (38) 117 (33). ^{1}H NMR ($CDCl_3$): δ 7.24 (m, 2H), 7.09 (d, $J = 8.5$ Hz, 2H), 7.04 (d, $J = 6.5$ Hz, 2H), 7.03 (d, $J = 6.5$ Hz, 2H), 6.89 (t, $J = 7$ Hz, 1 H), 5.94 (m, 1H), 5.64 (s, 1H), 5.06 (m, 2H), 3.34 (d, $J = 6.5$ Hz, 2H). ^{13}C NMR (CD_2Cl_2): δ 144.0, 141.4, 138.4, 133.3, 129.7, 129.6, 120.7, 118.7, 117.3, 115.5, 39.8. Elem anal. Calcd for $C_{15}H_{15}N$: C, 86.08; H, 7.22; N, 6.69. Found: C, 85.95; H, 7.11; N, 6.82.

Synthesis of 5,5′-Diiodo-2,2′-bithiophene (3). This modified synthesis (75, 76) was performed as detailed below. Sublimed I_2 (4.589 g, 1.808×10^{-2} mol) and the catalyst red HgO (3.909 g, 1.805×10^{-2} mol) were added alternatively, in small portions over a period of 1 h, to a stirring solution of bithiophene (1.536 g, 9.24×10^{-3} mol) in 40 mL of anhydrous benzene at 0 °C and then allowed to warm to room temperature and stir overnight. Another portion of I_2 (0.530 g, 2.09×10^{-3} mol) was next added at room temperature, and the red-orange solution was again allowed to stir overnight. The reaction mixture was then diluted with ~100 mL of $CHCl_3$ and washed with a saturated aqueous KI solution (3 × 20 mL) and a saturated aqueous sodium thiosulfate solution (3 × 20 mL) to remove excess I_2. The organic phase was then washed once with water and twice with brine and dried over $MgSO_4$. $MgSO_4$ was then removed by filtration, and the solvents were removed by rotary evaporation. Recrystallization of the residue from chloroform/ethanol (6:1) yielded 2.14 g of **3** as light tan crystals. The solvent was removed from the mother liquor via rotary evaporation, and the resultant solid yielded another 0.67 g of **3** after a second recrystallization, totaling 2.82 g (73% yield) of **3** as light tan crystals. GC/MS: single peak (rel intens) *m/z* 420 ($M^+ + 2H$, 9), 419 ($M^+ + H$, 10), 418 (M^+ 100), 291 (8), 247 (20), 164 (17). Mp: 164 °C. ^{1}H NMR ($CDCl_3$): δ 7.14 (d, $J = 3.5$ Hz, 2H), 6.78 (d, $J = 3.5$ Hz, 2H). Elem anal. Calcd for $C_8H_4S_2I_2$: C, 22.98; H, 0.96. Found: C, 23.08; H, 1.04.

Synthesis of 5,5′-Bis[(*p*-allylphenyl)phenylamino]-2,2′-bithiophene (4). $Pd_2(dba)_3$ (26.5 mg, 2.89×10^{-5} mol) and tri(*tert*-butyl)phosphine (6.5 mg, 3.2×10^{-5} mol) were weighed out in a glovebox and dissolved in ~5 mL of toluene. After stirring for ~5 min, these were added to a flask containing **2** (0.603 g, 2.88×10^{-3} mol), **3** (0.300 g, 7.16×10^{-4} mol), and sodium *tert*-butoxide (0.207 g, 2.15×10^{-3} mol) in ~80 mL of anhydrous, anaerobic toluene, the mixture was refluxed for 2 h until TLC (hexanes:toluene = 9:1), and GC/MS indicated that the reaction was complete. The mixture was then cooled to room temperature and filtered, and the solvent was removed in vacuo at <40 °C. The product was purified via column chromatography on silica gel deactivated with 2 wt % triethylamine using hexanes/toluene (9:1) as the eluent. The solvent was then removed in vacuo at <40 °C, leaving **4** as a strongly fluorescent yellow solid that was dried overnight under vacuum (0.195 g, 3.36×10^{-4} mol, 47% yield). MALDI: (rel intens) *m/z* 582.4 ($M^+ + 2H$, 39), 581.8 ($M^+ + H$, 77), 580.8 (M^+, 100). ^{1}H NMR (CD_2Cl_2): δ 7.46−6.96 (m, 22H), 5.95 (m, 2H), 5.06 (m, 4H), 3.37 (d, $J = 6.5$ Hz, 4H). Elem anal. Calcd for $C_{38}H_{32}N_2S_2$: C, 78.58; H, 5.55; N, 4.82. Found: C, 78.04; H, 5.68; N, 4.37.

Synthesis of 5,5′-Bis[(*p*-trichlorosilylpropylphenyl)phenylamino]-2,2′-bithiophene (5, PABTSi$_2$). Excess $HSiCl_3$ (0.09 mL, 8.609×10^{-4} mol) and a few grains of a dicyclopentadienylplatinum(II) chloride (Cp_2PtCl_2) catalyst were added in a glovebox to a solution of **4** (0.050 g, 8.609×10^{-5} mol) in about 10 mL of anhydrous toluene. The solution was transferred to a Schlenk line, where it was heated to 60 °C with stirring and left under static N_2 to prevent evaporation of $HSiCl_3$. The reaction progress was monitored by ^{1}H NMR, and the solution cooled to room temperature after 42 h. Toluene and excess $HSiCl_3$ were next removed in vacuo. Upon trituration of the crude product with 15 mL of a dry 1:1 toluene/pentane solution, a solid formed and was removed via cannula filtration. The supernatant was then removed in vacuo to yield a yellow solid **5** (0.072 g, 99% yield). ^{1}H NMR ($CDCl_3$): δ 7.40−6.90 (m, 22H), 2.68 (m, 4H), 1.83 (t, $J = 8.5$ Hz, 4H), 1.43 (t, $J = 8.5$ Hz, 4H). HRMS of $C_{38}H_{34}N_2S_2Si_2Cl_6$ (rel intens). Calcd: *m/z* 853.9739, 851.9769, 849.9798. Found: *m/z* 853.9734 (53.7), 851.9752 (93.5), 849.9779 (100).

TPDSi$_2$:TFB Film Deposition. $TPDSi_2$ and TFB were stored in sealed flasks in a N_2-filled glovebox as 10 mg/mL solutions, each in either dry toluene or dry CB. For film fabrication, $TPDSi_2$ + TFB solutions in the same solvent were combined in a 1:1 ratio and diluted to yield a solution of ~3 mg/mL of each component. To spin-coat films in the glovebox, this solution was passed through a 0.22 μm Teflon syringe filter onto cleaned ITO substrates, which were spun at 2000 rpm for 45 s. The films were then briefly exposed to air for ~5 min to promote hydrolysis/cross-linking of the trichlorosilane groups. The resultant ~10 nm films were subsequently annealed on a hot plate in the glovebox at 70 °C for 1 h prior to active-layer deposition.

PABTSi$_2$:TFB Film Deposition. $PABTSi_2$ was stored as a 10 mg/mL solution in a N_2-filled glovebox in either dry toluene or dry CB. For OPV fabrication, $PABTSi_2$ and TFB solutions in the same solvent were combined in the glovebox. To spin-coat films in the glovebox, the $PABTSi_2$ + TFB solution was passed through a 0.22 μm Teflon syringe filter onto cleaned ITO substrates. The films were then briefly exposed to air for ~5 min to promote hydrolysis/cross-linking of the trichlorosilane groups. The resultant films were subsequently annealed on a hot plate in the glovebox at 70 °C for 1 h prior to active-layer deposition. The solvent, solution concentration, ratio of components, spin-coating parameters, and annealing conditions were varied to obtain optimum OPV performance. Optimal device performance was achieved by spin-casting $PABTSi_2$:TFB (1:2) from a solution that was 1.68 mM in $PABTSi_2$ at 2000 rpm for 45 s.

Organic Field-Effect Transistor (OFET) Fabrication. Top-contact (staggered) OFETs were fabricated utilizing a ~20−30 nm $PABTSi_2$:TFB film derived from a 1:2 $PABTSi_2$:TFB solution in CB as the semiconducting layer. This layer was deposited via spin coating in a glovebox onto an n^+-Si/SiO_2 substrate (gate

Scheme 2. Synthetic Route to $PABTSi_2$

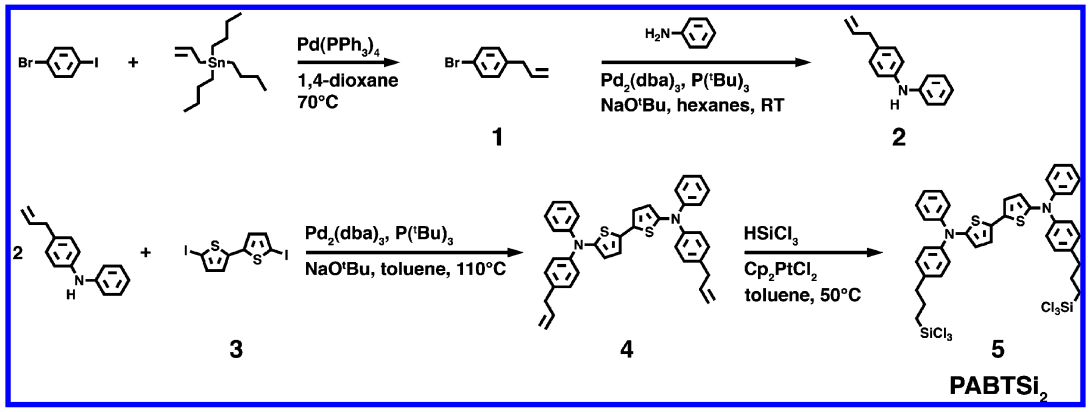

electrode) having a hexamethyldisilazane (HMDS)-treated SiO_2 dielectric layer. After exposure to ambient conditions and annealing to ensure $PABTSi_2$ cross-linking, the Au source and drain electrodes were vapor-deposited to create OFET devices with a channel length (L) and a width (W) of 100 and 1000 μm, respectively.

OPV Fabrication. Detailed descriptions of P3HT:PCBM (18) and MDMO-PPV:PCBM (25) device fabrication procedures can be found elsewhere. In brief, UV−ozone (UVO)-cleaned, patterned ITO substrates were coated with the appropriate IFL, and then either a P3HT:PCBM (1:1 by weight, ∼220 nm) or an MDMO-PPV:PCBM (1:4 by weight, ∼100 nm) active layer was spin-coated on top (60 s at 550 rpm or 45 s at 1500 rpm, respectively) in the glovebox and then annealed. If no IFL was to be used in the P3HT:PCBM devices, the ITO was treated with a dilute HCl solution prior to UVO treatment to increase the work function to 5.0 eV and enhance the performance (77). LiF/Al cathodes were sequentially deposited by thermal evaporation through a shadow mask without breaking vacuum to yield four devices per substrate, each with an active area of ∼0.060 ± 0.004 cm^2. The completed devices were encapsulated in the glovebox and tested under ambient conditions, as described elsewhere (18, 25).

Computational Methodology. Equilibrium geometry optimizations using density functional theory (DFT) with a B3LPY functional and the 6-31G* basis set were performed using *QChem 2.1* (78). Single-point calculations using these optimized geometries were performed at the DFT/B3LPY/6-31G* level of theory to obtain molecular orbital energies (*QChem*). Energy levels were adjusted to experimentally obtained electrochemical values for $TPDSi_2$ HOMO and LUMO energies (see the discussion below).

III. RESULTS AND DISCUSSION

This section first describes the design, synthesis, and characterization of $PABTSi_2$ as well as the morphological, optical, and electrochemical characteristics of $PABTSi_2$-based films. The consequences of implementing $PABTSi_2$:TFB-based IFLs in two well-characterized donor polymer:PCBM BHJ systems, using MDMO-PPV and P3HT (3, 14, 17, 22), are then presented. It will be seen that the $PABTSi_2$-derived IFL, having a HOMO well-aligned energetically with that of P3HT, functions as an efficient HTL/EBL when paired with a P3HT:PCBM active layer but not with an MDMO-PPV:PCBM active layer. These disparities are primarily attributed to differences in energy level matching and underscore the significance of tailoring IFL electronic properties to those of the associated OPV active material.

$PABTSi_2$ Design. Using geometries optimized at the DFT/B3LYP/3-21G* level, HOMO and LUMO energy calculations targeted $TPDSi_2$ modifications required to raise the HOMO energy to better match that of P3HT while maintaining a sufficiently high LUMO to block misdirected electrons as an anode IFL. Appending alkoxy electron donors to the TPD phenyl para position is known to raise the HOMO only slightly (79). In contrast, bithiophene fragments are significantly more electron-rich, leading to higher-lying HOMOs (71, 80, 81). The present B3LYP/6-31G* level calculations predict $PABTSi_2$ HOMO and LUMO energies of 4.9 and 1.7 eV, respectively, versus 5.3 and 2.3 eV for $TPDSi_2$. These will be shown below to be in good agreement with experimental CV and optical spectroscopy results. These data are also in good agreement with literature electrochemical data for similar p-type architectures without propyltrichlorosilane tethers (82). Such functionalized "tethers" are essential for $PABTSi_2$ covalent chemisorption on the ITO surface (83−85) and for the formation of cross-linked IFL blends in air. This renders the IFL film insoluble in standard organic solvents and thus facilitates the BHJ OPV fabrication, without significantly compromising the frontier orbital energetics.

$PABTSi_2$ Synthesis. Initially, a synthetic route analogous to that for $TPDSi_2$ (43) was pursued using a bithiophene rather than a biphenyl core, beginning with Buchwald−Hartwig coupling (86−91) of aniline and 5,5′-dibromo-2,2′-bithiophene. Although a variety of catalysts, ligands, and reaction conditions were investigated, negligible yields were obtained. This agrees with the general findings that while 2-bromobithiophene coupling with secondary amines proceeds in high yield, negligible reaction is observed with aniline (92). The successful $PABTSi_2$ synthetic pathway then adopted is that in Scheme 2, and details are provided in the Experimental Section.

$PABTSi_2$ Film Characterization. The morphological, electrochemical, and optical properties of the $PABTSi_2$-derived and $PABTSi_2$:TFB-derived films were characterized by AFM, CV, and optical spectroscopy, and the results are compared below to those for $TPDSi_2$.

Cross-linked Film Morphology. $PABTSi_2$ and $PABTSi_2$:TFB films were spin-coated from either a toluene or CB solution and thermally cured as indicated in the Experimen-

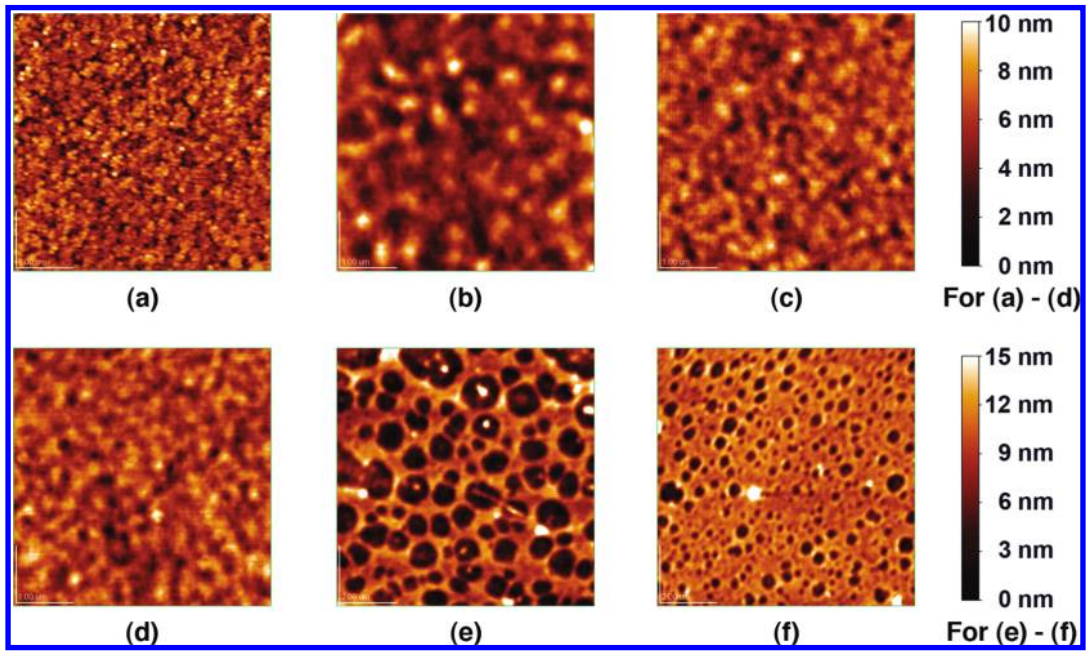

FIGURE 3. Tapping-mode AFM images of (a) bare ITO (rms roughness = 1.4 nm), (b) an unannealed $PABTSi_2$-derived film spin-coated from toluene (0.7 nm); (c) an unannealed $PABTSi_2$:TFB (1:1)-derived film spin-coated from toluene (0.5 nm); (d) 135 °C-annealed $PABTSi_2$:TFB (1:1)-derived film spin-coated from toluene (0.6 nm); (e) 135 °C-annealed $PABTSi_2$:TFB (1:1)-derived film spin-coated from CB (3.2 nm); (f) 135 °C-annealed $PABTSi_2$:TFB (1:2)-derived film spin-coated from CB (2.2 nm). Scans a−d are 4.5 × 4.5 μm images with height (z) = 0−10 nm; scans e and f are 9 × 9 μm images with z = 0−15 nm.

tal Section. Tapping-mode AFM images of the resulting films on ITO (typical ITO rms roughness ≈ 1.4 nm; Figure 3a) reveal planarization of the ITO surface upon $PABTSi_2$ and $PABTSi_2$:TFB film deposition from toluene, similar to the results for $TPDSi_2$ and $TPDSi_2$:TFB (42, 43, 93). Figure 3b shows a smooth (rms roughness = 0.7 nm), cross-linked, unannealed $PABTSi_2$ film cast from toluene, while Figure 3c demonstrates that incorporating an equal amount of TFB yields even smoother cross-linked films (rms roughness = 0.5 nm). Annealing the films at various temperatures in a N_2 glovebox for 1 h produces no significant change in the $PABTSi_2$:TFB morphology, as exemplified by the specimen in Figure 3d (rms roughness = 0.6 nm), which was annealed at 135 °C. Note that if CB is used as the spin-casting solvent, $PABTSi_2$:TFB films exhibit rougher surfaces (rms roughness = 3.2 nm) with obvious phase-separation features of ∼0.5−1.0 μm (Figure 3e). In CB-cast films, changing the component ratio to 1:2 $PABTSi_2$:TFB yields smoother, more homogeneous films than does the 1:1 ratio, now affording phase-separation features of ∼300−500 nm with rms roughness = 2.2 nm (Figure 3f). Line scans of Figure 3e,f (see the Supporting Information) reveal the height variation between the different phases to be ∼10 nm, which is less than half of the thickness of the 25 nm films, indicating that the film achieves complete ITO coverage. OPV fabrication experiments indicate that CB solutions are required for the P3HT:PCBM active layers to completely wet the IFL surface and that annealed 1:2 $PABTSi_2$:TFB films from CB (Figure 3f) afford the highest-performing P3HT:PCBM OPVs (see below).

Comparative Electrochemical Properties of $PABTSi_2$- and $TPDSi_2$-Based Films. The electrochemical response of $PABTSi_2$- and $TPDSi_2$-derived films was

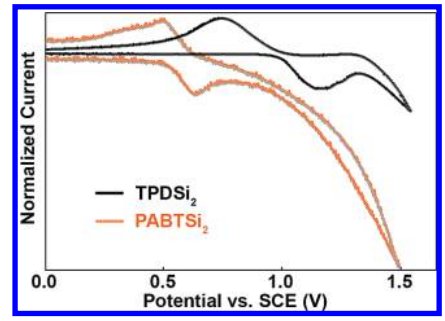

FIGURE 4. Cyclic voltammograms of $TPDSi_2$ and $PABTSi_2$ drop-cast films on a platinum electrode in acetonitrile with 0.1 M $Bu_4N^+PF_6^-$ as the electrolyte. Scan rates are 100 mV/s.

investigated via CV (Figure 4). The onset of $TPDSi_2$ oxidation is 0.94 V (vs SCE), and the separation of the reversible half-wave energies (ΔE) is quite large (∼400 mV). $PABTSi_2$ exhibits the onset of oxidation around 0.50 V, also with a large separation of forward and reverse peaks (∼150 mV). It is evident that the bithiophene core affords a more electron-rich IFL and raises the HOMO level closer to vacuum for closer alignment with the P3HT HOMO. The $TPDSi_2$ and $PABTSi_2$ HOMO energies as determined electrochemically are 5.3 and 4.9 eV, respectively, and are shown in relation to the MDMO-PPV and P3HT HOMO energies in Figure 2. Because the P3HT HOMO is ∼5.0 eV, $PABTSi_2$ has excellent energy-level alignment to accept holes from this BHJ polymer en route to collection at the ITO anode. It will be shown below that films produced by blending $PABTSi_2$ with TFB are p-type semiconductors with substantial FET hole mobility. In contrast, $TPDSi_2$-derived films are expected to be less efficient in hole collection from the P3HT because of the deeper-lying HOMO and, when blended with TFB, exhibit somewhat lower FET hole mobility.

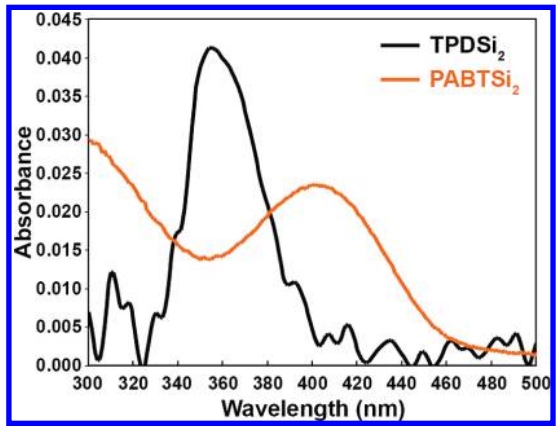

FIGURE 5. Optical absorption characteristics of spin-cast films of $PABTSi_2$ (~20 nm) and $TPDSi_2$ (~10 nm) on glass substrates.

Additional information is gleaned from the electrochemistry by noting that the expected 59 mV ΔE values for Nernstian reactions in solution, and for rapid reversible electron transfer, are not observed here (94). Larger half-wave spacings typical of some surface-anchored species and observed for the $TPDSi_2$- and $PABTSi_2$-based films can be attributed to densely cross-linked films in which redox processes are kinetically hindered, likely via impeded counteranion mobility through the dense matrices (69, 85, 94).

Optical Spectroscopy of $PABTSi_2$- and $TPDSi_2$-Derived Films. An important OPV IFL requirement is optical transparency to ensure that the maximum photon flux reaches the active layer. Figure 5 illustrates that both $PABTSi_2$- and $TPDSi_2$-derived films exhibit good optical transparency in the visible region, with maximum absorption peaks (λ_{max}) at 401 and 355 nm, respectively. Importantly, neither cross-section interferes significantly with the P3HT (λ_{max} = 493–517 nm, shoulder at 572 nm) or MDMO-PPV (λ_{max} = 500 nm) film absorption (95, 96). Additionally, the solar spectral region with the largest photon flux is in wavelengths equal to or longer than that absorbed by the present active-layer materials, and a relatively small percentage of solar photons (~15%) is even of proper energy for IFL absorption (4). Moreover, the IFLs applied to the present OPV devices are only ~10–25 nm in thickness, so that the absorbance of the $TPDSi_2$- and $PABTSi_2$-derived films at λ_{max} is only ~0.02–0.04 absorbance units, corresponding to 91–95% transmission at λ_{max}. The LUMO energies for $PABTSi_2$ and $TPDSi_2$, estimated from the optical band gap, as determined from the onset of absorption and the CV-derived HOMO values, are 2.2 and 2.3 eV, respectively.

Solubility of $PABTSi_2$:TFB-Derived IFLs. Optical spectra of a blended, spin-cast, cross-linked $PABTSi_2$:TFB film before and after soaking in CB for ~1 min (Figure 6a) demonstrate that the present film deposition process embeds TFB within a cross-linked $PABTSi_2$ matrix, rendering both film components insoluble in common organic solvents. This insolubility, demonstrated by cross-linked $PABTSi_2$ and $TPDSi_2$ (15, 42), is pivotal in utilizing these as IFLs because the successive spin-coating procedures required in BHJ device fabrication necessitate that the deposition of one layer not dissolve the previous one. In the past, this was achieved using orthogonal solvents, such as for aqueous PEDOT:PSS suspensions. In contrast to cross-linked $PABTSi_2$:TFB, neat TFB films dissolve readily upon exposure to CB for only several seconds (Figure 6b).

IFL Transport Properties. Maintaining sufficient and balanced BHJ hole and electron mobilities is important to prevent space charge from building up and eroding OPV power conversion efficiency (3, 97). It is similarly important that an anode-side IFL, such as the present $PABTSi_2$:TFB-derived films, exhibit significant hole mobility to prevent charge buildup at this interface. Thus, the FET hole mobility (μ_h) of $PABTSi_2$:TFB films was measured and compared to parallel results for $TPDSi_2$:TFB (98). Top-contact OFET devices (98) were fabricated having the structure n^+-Si (gate)/SiO_2-HMDS (300 nm)/$PABTSi_2$:TFB film (20–30 nm)/Au source drain (50 nm) with L = 100 μm and W = 1000 μm. The hole mobility of $PABTSi_2$:TFB was determined to be 1.1 × 10^{-3} $cm^2/V \cdot s$, the current on–off ratio (I_{on}:I_{off}) ~10^5, and the threshold voltage (V_T) −14 V. These metrics are comparable to, or slightly better than, those for $TPDSi_2$:TFB and TFB alone (Table 1).

OPV Device Performance Using $PABTSi_2$:TFB as an IFL. BHJ OPV devices containing P3HT:PCBM and MDMO-PPV:PCBM active layers and utilizing $PABTSi_2$:TFB, $TPDSi_2$:TFB, and PEDOT:PSS IFLs between the ITO and the

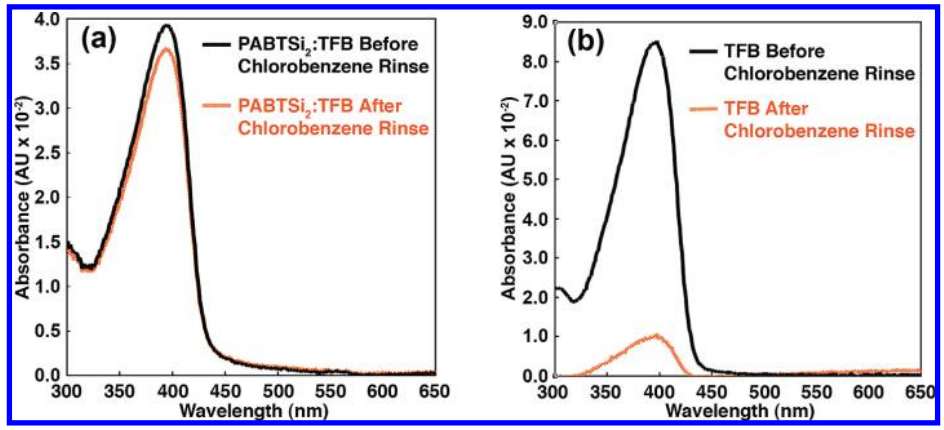

FIGURE 6. Transmission optical spectra demonstrate that (a) ~10 nm $PABTSi_2$:TFB-based films are insoluble in CB and that (b) ~20 nm pure TFB films are readily dissolved by CB.

Table 1. OFET Performance of Semiconductors PABTSi$_2$:TFB, TPDSi$_2$:TFB, and TFB in a (Staggered) Bottom-Gate, Top-Contact Architecture

semiconductor	μ_h[a]	I_{on}:I_{off}	V_T[b]
PABTSi$_2$:TFB	1.1×10^{-3}	10^5	−14
TPDSi$_2$:TFB[c]	5×10^{-4}	10^4	−15
TFB[c]	8×10^{-4}	10^5	−30

[a] Units of cm^2/V · s. [b] Units of V. [c] Data from ref 98.

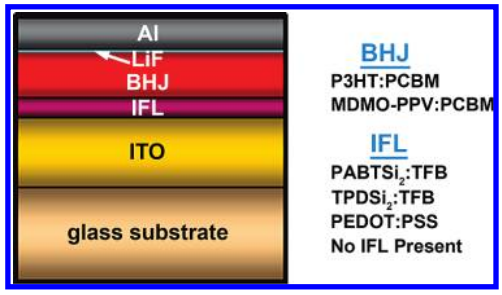

FIGURE 7. OPV device architecture with a P3HT:PCBM or MDMO-PPV:PCBM BHJ active layer and a PABTSi$_2$:TFB, TPDSi$_2$:TFB, or PEDOT:PSS IFL (99).

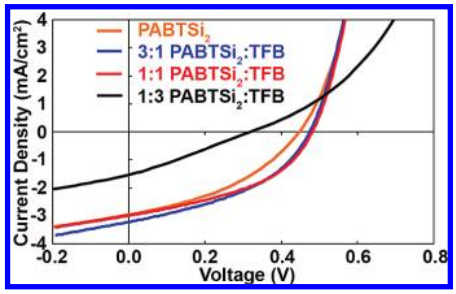

FIGURE 8. $J-V$ plots for BHJ OPVs having MDMO-PPV:PCBM active layers with various ratios of the PABTSi$_2$:TFB IFL components. Data plotted are for individual representative devices with typical performance metrics for their respective architectures and materials composition.

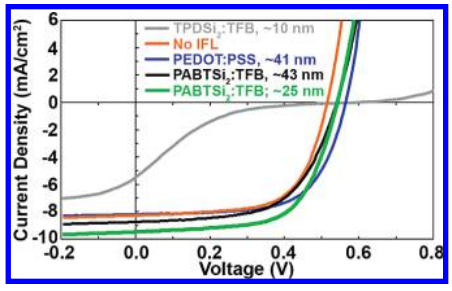

FIGURE 9. $J-V$ plots for BHJ OPVs having a P3HT:PCBM active layer fabricated with the indicated IFLs, including various IFL PABTSi$_2$:TFB (1:2) IFL thicknesses. Data plotted are for individual representative devices with typical performance metrics for their respective architectures and materials composition.

BHJ layer were fabricated as shown in Figure 7. Figures 8 and 9 show current density−voltage ($J-V$) plots for these cells, and data are summarized in Tables 2 and 3.

PABTSi$_2$ IFLs in MDMO-PPV:PCBM OPVs. OPVs with MDMO-PPV as the donor polymer were previously shown to exhibit enhanced V_{oc} and η_p metrics if a thin ∼10 nm TPDSi$_2$:TFB film is used as the IFL rather than conventional PEDOT:PSS (15, 25). The MDMO-PPV HOMO level (5.3 eV) aligns well with that of TPDSi$_2$ (Figure 2); a priori there should be little energetic barrier for hole transfer to the IFL and subsequent extraction by the ITO anode. Because TPDSi$_2$:TFB forms thermally robust, cross-linked films and OPVs having superior device performance versus those fabricated with PEDOT:PSS, TPDSi$_2$:TFB effectively replaces PEDOT:PSS in MDMO-PPV OPVs (15, 25). Substituting PABTSi$_2$ for TPDSi$_2$ while maintaining a constant active layer, however, does not afford significant performance improvement.

ITO/PABTSi$_2$:TFB/MDMO-PPV:PCBM/LiF/Al devices exhibit low V_{oc} values, similar to OPVs with no IFL (Figure 8 and Table 2). The origin of the low V_{oc} is likely nonohmic contact with the active layer. Mihailetchi et al. showed that, for BHJ OPVs with nonohmic contacts, V_{oc} is predominantly determined by the anode−cathode work function differential instead of the donor HOMO−acceptor LUMO separation (3, 100). The PABTSi$_2$ HOMO is not well-aligned with that of MDMO-PPV (∼0.4 eV difference; Figure 2), and the measured V_{oc} in PABTSi$_2$ cells is ∼0.47 V. Note that this value is identical with V_{oc} of ITO/MDMO-PPV:PCBM/LiF/Al devices having no anode IFL, which doubtless form a nonohmic anode-side contact due to the large MDMO-PPV HOMO (5.3 eV) and ITO work function (4.7 eV) energetic disparity. Additionally, the approximate work function differential of the ITO and Al electrodes ($\Delta\Phi = \Phi_{ITO} - \Phi_{Al} = 4.7$ eV − 4.2 eV = 0.5 eV), which should dictate V_{oc} in a device with a nonohmic contact, agrees well with the observed V_{oc}. These results all strongly suggest that a nonohmic contact is present at the MDMO-PPV OPV anode. Furthermore, cells using various PABTSi$_2$:TFB ratios of uniform film thickness (∼12 nm) yield OPVs with essentially invariant V_{oc} values of ∼0.47 V (Figure 8). As the ratio approaches 1:3 PABTSi$_2$:TFB, the measured series resistance (R_s) increases significantly, as is evident from the decreased $J-V$ plot slope near the x-axis intercept (Figure 8) and greatly reduced FF (6, 7, 101, 102). This result suggests that when there is insufficient silane to completely embed the TFB in a cross-linked matrix, a less dense IFL and an irregular interface results.

PABTSi$_2$ IFLs in P3HT:PCBM OPVs. The question next arises as to whether MDMO-PPV:PCBM active layers, known to have nanocrystalline PCBM domains and amorphous MDMO-PPV regions (103), interact differently than do P3HT:PCBM active layers with more ordered constituents (103, 104). In addition to the crystallinity variations, the two active layers, of course, have greatly different morphologies and donor orbital energetics, which should impart different interfacial and transport characteristics (105, 106). Such experiments require separate IFL optimizations for each active layer. For TPDSi$_2$:TFB and PABTSi$_2$:TFB in MDMO-PPV:PCBM OPVs, the optimum solvent used for spin coating of the IFL components is found to be toluene, as discussed above. Smooth films are obtained in this way as assessed by AFM, and MDMO-PPV:PCBM active-layer films cast from CB are also smooth. However, P3HT:PCBM active layers are typically spin-coated from more polar ODCB. In this work, it was found that ODCB-cast P3HT:PCBM layers dewet during the slow-drying process if deposited on toluene-cast IFLs, leaving only discontinuous BHJ areas on the substrate.

Table 2. Average Response Parameters and Standard Deviations (σ) for Several (Typically Four) ITO/PABTSi$_2$:TFB/MDMO-PPV:PCBM/LiF/Al OPV Devices Made in Parallel Having the PABTSi$_2$:TFB Ratios Indicated

	PABTSi$_2$:TFB ratio (σ)				
	0:0, no IFL	1:0	3:1	1:1	1:3
V_{oc} (V)	0.47 (0.04)	0.43 (0.02)	0.47 (0.01)	0.48 (0.004)	0.28 (0.02)
J_{sc} (mA/cm^2)	3.64 (0.17)	2.78 (0.27)	3.11 (0.16)	2.99 (0.12)	1.27 (0.18)
FF (%)	40.8 (0.5)	36.7 (1.7)	40.8 (1.2)	42.0 (0.7)	27.7 (1.7)
η_p (%)	0.71 (0.10)	0.40 (0.06)	0.60 (0.02)	0.60 (0.03)	0.10 (0.02)

Table 3. Average Response Parameters and Standard Deviations (σ) for Several (Typically Four) ITO/IFL/P3HT:PCBM/LiF/Al OPV Devices Having the Indicated IFLs, IFL Ratios, and IFL Thicknesses

	IFL used, ratio, thickness (σ)				
	PABTSi$_2$:TFB, 1:2, 25 nm	PABTSi$_2$:TFB, 1:2, 43 nm	PEDOT:PSS, 1:6, 41 nm	no IFL, 0:0, 0 nm	TPDSi$_2$:TFB, 1:1, 10 nm
V_{oc} (V)	0.54 (0.003)	0.54 (0.001)	0.56 (0.001)	0.52 (0.005)	0.55 (0.04)
J_{sc} (mA/cm^2)	9.31 (0.17)	8.40 (0.23)	8.57 (0.47)	8.04 (0.19)	4.72 (0.50)
FF (%)	62.7 (0.5)	59.3 (0.28)	65.1 (0.31)	64.4 (0.18)	10.4 (0.58)
η_p (%)	3.14 (0.08)	2.68 (0.08)	3.14 (0.17)	2.69 (0.03)	0.28 (0.04)

Thus, the IFL components were deposited from CB solutions, a solvent more compatible with ODCB, which significantly improves the IFL wetting by the P3HT:PCBM solutions, affording contiguous films.

The BHJ spin-casting solvent is known to have a significant impact on resultant film morphologies, as demonstrated previously for MDMO-PPV:PCBM active layers deposited from toluene and CB (14). Toluene-cast films afford rougher surfaces with large horizontal areas of phase segregation and yield lower-performing MDMO-PPV:PCBM OPVs than smoother CB-cast films, which exhibit more uniform constituent mixing. This characteristic allowed Shaheen et al. to increase the MDMO-PPV:PCBM OPV η_P from 0.9% to 2.5% by processing from CB rather than toluene (14). Similarly, the present PABTSi$_2$:TFB IFL morphologies for films cast from toluene versus CB are quite different, as illustrated in Figure 3d–f. CB affords rougher, more phase-segregated films than toluene, with apparent PABTSi$_2$ domain sizes of ~0.5–1 μm for a 1:1 PABTSi$_2$:TFB ratio and ~300–500 nm for a 1:2 ratio. Experimentation determined that a 1:2 ratio from CB affords optimum P3HT:PCBM BHJ OPV performance.

After optimization of the spin-coating solvent and IFL component ratio, the PABTSi$_2$:TFB film thicknesses were varied in P3HT:PCBM OPV fabrication. Not unexpectedly, increasing the thickness increases the overall OPV R_s (107, 108), determined from the inverse of the $J-V$ curve slope at the x-axis intercept and by the FF (6, 7, 101, 102). Figure 9 compares $J-V$ plots of several PABTSi$_2$:TFB film thicknesses to those of P3HT:PCBM devices using PEDOT:PSS and TPDSi$_2$:TFB as IFLs and also to a device having no IFL. All OPVs were fabricated in parallel, and it is evident that PABTSi$_2$:TFB produces OPV metrics rivaling optimized PEDOT:PSS devices. Response parameters from Figure 9 are compiled in Table 3. In the case of P3HT:PCBM OPVs with no IFL, a V_{oc} of 0.47 V is not observed, as for MDMO-PPV:PCBM devices with no IFL. The observed V_{oc} values for this P3HT:PCBM cell are only slightly less than devices that employ an IFL, implying that the anode contact for P3HT:PCBM OPVs without an IFL is still largely ohmic and V_{oc} is still determined predominantly by the HOMO–LUMO gap. This is likely attributable to the dilute HCl solution treatment that is known to optimize the IFL-free P3HT:PCBM device performance (77).

Note here that P3HT:PCBM devices fabricated with TPDSi$_2$:TFB IFLs perform marginally, using any deposition solvent, component ratio, or thickness investigated. Results for the optimized TPDSi$_2$:TFB/P3HT:PCBM devices are shown in Figure 9. We attribute this marginal TPDSi$_2$:TFB performance, as discussed above, to the large TPDSi$_2$ and P3HT HOMO energy mismatch, which creates a barrier to hole transport to, and collection at, the anode. This result also validates the rationale underlying the design and implementation of PABTSi$_2$-based IFLs for P3HT:PCBM BHJ OPVs as an effective cross-linking, hole-transporting bithiophene semiconductor with a HOMO energy closely aligned with that of P3HT.

IV. CONCLUSIONS

This contribution describes the synthesis, characterization, and implementation of an energetically tuned IFL precursor, PABTSi$_2$, as a component in P3HT:PCBM BHJ OPVs. Theory-aided design introduces a more electron-rich bithiophene, which effectively raises the HOMO energy to minimize the energy barrier for hole transfer between the PABTSi$_2$ IFL (4.9 eV) and P3HT (5.0 eV) while blocking misdirected electrons. Characterization data suggest that the PABTSi$_2$ HOMO (4.9 eV) is tailored perfectly for P3HT:PCBM-based OPVs, similar to TPDSi$_2$ IFLs for MDMO-PPV:PCBM-based OPVs. The robust, cross-linked PABTSi$_2$:TFB IFL strongly binds to the hydroxylated ITO surface, was incorporated into P3HT:PCBM OPVs, and affords optimized devices with solar power conversion efficiencies comparable to those of heavily optimized PEDOT:PSS-based devices.

Acknowledgment. We thank the DOE (Grant DE-FG02-08ER46536/A000) and ONR (Grants N000140810923 and

N000140510021) for support of this research and the Northwestern MRSEC (NSF Grant DMR-0520513) for providing characterization facilities. We also thank Dr. A. Facchetti, Dr. H. Usta, and Dr. H. Huang for helpful discussions, S. Shafaie for HRMS measurements, and C. Kim for assistance with OFET characterization.

Supporting Information Available: Line scans of AFM images. This material is available free of charge via the Internet at http://pubs.acs.org.

REFERENCES AND NOTES

(1) Dennler, G.; Scharber, M. C.; Brabec, C. J. *Adv. Mater.* **2009**, *21*, 1.
(2) Jørgensen, M.; Norrman, K.; Krebs, F. C. *Sol. Energy Mater. Sol. Cells* **2008**, *92*, 686.
(3) Blom, P. W. M.; Mihailetchi, V. D.; Koster, L. J. A.; Markov, D. E. *Adv. Mater.* **2007**, *19*, 1551.
(4) Bundgaard, E.; Krebs, F. C. *Sol. Energy Mater. Sol. Cells* **2007**, *91*, 954.
(5) Günes, S.; Neugebauer, H.; Sariciftci, N. S. *Chem. Rev.* **2007**, *107*, 1324.
(6) Rand, B. P.; Genoe, J.; Heremans, P.; Poortmans, J. *Prog. Photovolt. Res. Appl.* **2007**, *15*, 659.
(7) Moliton, A.; Nunzi, J.-M. *Polym. Int.* **2006**, *55*, 583.
(8) Gledhill, S. E.; Scott, B.; Gregg, B. A. *J. Mater. Res.* **2005**, *20*, 3167.
(9) Sun, S.-S.; Sariciftci, N. S. *Organic Photovoltaics: Mechanisms, Materials, and Devices*; CRC: Boca Raton, FL, 2005.
(10) Tang, C. W. *Appl. Phys. Lett.* **1986**, *48*, 183.
(11) Halls, J. J. M.; Walsh, C. A.; Greenham, N. C.; Marseglia, E. A.; Friend, R. H.; Moratti, S. C.; Holmes, A. B. *Nature* **1995**, *376*, 498.
(12) Yu, G.; Gao, J.; Hummelen, J. C.; Wudl, F.; Heeger, A. J. *Science* **1995**, *270*, 1789.
(13) Yu, G.; Heeger, A. J. *J. Appl. Phys.* **1995**, *78*, 4510.
(14) Shaheen, S. E.; Brabec, C. J.; Sariciftci, N. S.; Padinger, F.; Fromherz, T.; Hummelen, J. C. *Appl. Phys. Lett.* **2001**, *78*, 841.
(15) Hains, A. W.; Marks, T. J. *Appl. Phys. Lett.* **2008**, *92*, 023504.
(16) Li, G.; Shrotriya, V.; Huang, J.; Yao, Y.; Moriarty, T.; Emery, K.; Yang, Y. *Nat. Mater.* **2005**, *4*, 864.
(17) Ma, W.; Yang, C.; Gong, X.; Kwanghee, L.; Heeger, A. *Adv. Funct. Mater.* **2005**, *15*, 1617.
(18) Irwin, M. D.; Buchholz, D. B.; Hains, A. W.; Chang, R. P. H.; Marks, T. J. *Proc. Natl. Acad. Sci. U.S.A.* **2008**, *105*, 2783.
(19) Green, M. A.; Emery, K.; Hishikawa, Y.; Warta, W. *Prog. Photovolt. Res. Appl.* **2009**, *17*, 85.
(20) Koster, L. J. A.; Mihailetchi, V. D.; Blom, P. W. M. *Appl. Phys. Lett.* **2006**, *88*, 093511.
(21) Rand, B. P.; Burk, D. P.; Forrest, S. R. *Phys. Rev. B: Condens. Matter* **2007**, *75*, 115327.
(22) Dennler, G.; Scharber, M. C.; Ameri, T.; Denk, P.; Forberich, K.; Waldauf, C.; Brabec, C. J. *Adv. Mater.* **2008**, *20*, 579.
(23) Scharber, M. C.; Mühlbacher, D.; Koppe, M.; Denk, P.; Waldauf, C.; Heeger, A. J.; Brabec, C. J. *Adv. Mater.* **2006**, *18*, 789.
(24) Brabec, C. J.; Hauch, J. A.; Schilinsky, P.; Waldauf, C. *MRS Bull.* **2005**, *30*, 50.
(25) Hains, A. W.; Liu, J.; Martinson, A. B. F.; Irwin, M. D.; Marks, T. J. *Adv. Funct. Mater.* **2009**, in press.
(26) Liu, A.; Zhao, S.; Rim, S.-B.; Wu, J.; Könemann, M.; Erk, P.; Peumans, P. *Adv. Mater.* **2008**, *20*, 1065.
(27) Gregg, B. A. *J. Phys. Chem. B* **2003**, *107*, 4688.
(28) Gregg, B. A. *MRS Bull.* **2005**, *30*, 20.
(29) Lin, Z. *Chem.—Eur. J.* **2008**, *14*, 6494.
(30) Nanditha, D. M.; Dissanayake, M.; Hatton, R. A.; Curry, R. J.; Silva, S. R. P. *Appl. Phys. Lett.* **2007**, *90*, 113505.
(31) Kim, J. Y.; Lee, K.; Coates, N. E.; Moses, D.; Nguyen, T.-Q.; Dante, M.; Heeger, A. J. *Science* **2007**, *317*, 222.
(32) Kim, J. Y.; Kim, S. H.; Lee, H.-H.; Lee, K.; Ma, W.; Gong, X.; Heeger, A. J. *Adv. Mater.* **2006**, *18*, 572.
(33) Verlaak, S.; Arkhipov, V.; Heremans, P. *Appl. Phys. Lett.* **2003**, *82*, 745.
(34) Wang, D.; Reese, M.; Kopidakis, N.; Gregg, B. A. Do the defects make it work? Defect engineering in pi-conjugated polymers and their solar cells. *33rd IEEE Photovoltaic Specialists Conference*, San Diego, CA, 2008; IEEE: Pittsburgh, PA, 2008; p 1.
(35) Peumans, P.; Forrest, S. R. *Chem. Phys. Lett.* **2004**, *398*, 27.
(36) Reese, M. O.; Morfa, A. J.; White, M. S.; Kopidakis, N.; Shaheen, S. E.; Rumbles, G.; Ginley, D. S. *Sol. Energy Mater. Sol. Cells* **2008**, *92*, 746.
(37) Shaheen, S. E. Mechanisms of Operation and Degradation in Solution-Processable Organic Photovoltaics. *IEEE 45th Annual International Reliability Physics Symposium*, Phoenix, AZ, 2007; IEEE: Pittsburgh, PA, 2007; p 1.
(38) Koetse, M. M.; Sweelssen, J.; Franse, T.; Veenstra, S. C.; Kroon, J. M.; Yang, X.; Alexeev, A.; Loos, J.; Schubert, U. S.; Schoo, H. F. M. *Proc. SPIE: Int. Soc. Opt. Eng.* **2004**, *5215*, 119.
(39) Xu, M. S.; Xu, J. B. *J. Phys. D: Appl. Phys.* **2004**, *37*, 1603.
(40) Paniagua, S. A.; Hotchkiss, P. J.; Jones, S. C.; Marder, S. R.; Mudalige, A.; Marrikar, F. S.; Pemberton, J. E.; Armstrong, N. R. *J. Phys. Chem. C* **2008**, *112*, 7809.
(41) Li, Z. R.; Meng, H. *Organic Light-Emitting Materials and Devices*; CRC: Boca Raton, FL, 2006.
(42) Yan, H.; Lee, P.; Armstrong, N. R.; Graham, A.; Evmenenko, G. A.; Dutta, P.; Marks, T. J. *J. Am. Chem. Soc.* **2005**, *127*, 3172.
(43) Huang, Q.; Evmenenko, G. A.; Dutta, P.; Lee, P.; Armstrong, N. R.; Marks, T. J. *J. Am. Chem. Soc.* **2005**, *127*, 10227.
(44) Adamovich, V.; Brooks, J.; Tamayo, A.; Alexander, A. M.; Djurovich, P. I.; D'Andrade, B. W.; Adachi, C.; Forrest, S. R.; Thompson, M. E. *New J. Chem.* **2002**, *26*, 1171.
(45) Irwin, M. D.; Buchholz, D. B.; Leever, B. J.; Liu, J.; Emery, J. D.; Zhang, M.; Song, J.-H.; Durstock, M. F.; Freeman, A. J.; Bedzyk, M. J.; Hersam, M. C.; Chang, R. P. H.; Marks, T. J. *J. Am. Chem. Soc.* **2009**, in press.
(46) Rider, D. A.; Harris, K. D.; Wang, D.; Bruce, J.; Fleischauer, M. D.; Tucker, R. T.; Brett, M. J.; Bruiak, J. M. *ACS Appl. Mater. Interfaces* **2009**, *1*, 279.
(47) Li, N.; Lassiter, B. E.; Lunt, R. R.; Wei, G.; Forrest, S. R. *Appl. Phys. Lett.* **2009**, *94*, 023307.
(48) Kim, D. Y.; Subbiah, J.; Sarasqueta, G.; So, F.; Ding, H.; Irfan; Gao, Y. *Appl. Phys. Lett.* **2009**, *95*, 093304.
(49) Yamakawa, S.; Tajima, K.; Hashimoto, K. *Org. Electron.* **2009**, *10*, 511.
(50) Kang, B.; Tan, L. W.; Silva, S. R. P. *Appl. Phys. Lett.* **2008**, *93*, 133302.
(51) Hwang, E.; da Silva, K. M. N.; Seevers, C. B.; Li, J.-R.; Garno, J. C.; Nesterov, E. E. *Langmuir* **2008**, *24*, 9700.
(52) Marrikar, F. S.; Brumbach, M.; Evans, D. H.; Lebrón-Paler, A.; Pemberton, J. E.; Wysocki, R. J.; Armstrong, N. R. *Langmuir* **2007**, *23*, 1530.
(53) Shrotriya, V.; Li, G.; Yao, Y.; Chu, C.-W.; Yang, Y. *Appl. Phys. Lett.* **2006**, *88*, 073508.
(54) Brabec, C. J.; Shaheen, S. E.; Winder, C.; Sariciftci, N. S. *Appl. Phys. Lett.* **2002**, *80*, 1288.
(55) Ahlswede, E.; Hanisch, J.; Powalla, M. *Appl. Phys. Lett.* **2007**, *90*, 163504.
(56) Li, G.; Chu, C.-W.; Shrotriya, V.; Huang, J.; Yang, Y. *Appl. Phys. Lett.* **2006**, *88*, 253503.
(57) Peumans, P.; Forrest, S. R. *Appl. Phys. Lett.* **2001**, *79*, 126.
(58) Lee, T.-W.; Chung, Y. *Adv. Funct. Mater.* **2008**, *18*, 2246.
(59) de Kok, M. M.; Buechel, M.; Vulto, S. I. E.; van de Weijer, P.; Meulenkamp, E. A.; de Winter, S. H. P. M.; Mank, A. J. G.; Vorstenbosch, H. J. M.; Weijtens, C. H. L.; van Elsbergen, V. *Phys. Status Solidi A* **2004**, *201*, 1342.
(60) Brown, T. M.; Kim, J. S.; Friend, R. H.; Cacialli, F.; Daik, R.; Feast, W. J. *Appl. Phys. Lett.* **1999**, *75*, 1679.
(61) Kemerink, M.; Timpanaro, S.; de Kok, M. M.; Meulenkamp, E. A.; Touwslager, F. J. *J. Phys. Chem. B* **2004**, *108*, 18820.
(62) Ionescu-Zanetti, C.; Mechler, A.; Carter, S. A.; Lal, R. *Adv. Mater.* **2004**, *16*, 385.
(63) de Jong, M. P.; van IJzendoorn, L. J.; de Voigt, M. J. A. *Appl. Phys. Lett.* **2000**, *77*, 2255.
(64) Wong, K. W.; Yip, H. L.; Luo, Y.; Wong, K. Y.; Lau, W. M.; Low, K. H.; Chow, H. F.; Gao, Z. Q.; Yeung, L.; Chang, C. C. *Appl. Phys. Lett.* **2002**, *80*, 2788.
(65) Ni, J.; Yan, H.; Wang, A.; Yang, Y.; Stern, C. L.; Metz, A. W.; Jin, S.; Wang, L.; Marks, T. J.; Ireland, J. R.; Kannewurf, C. R. *J. Am. Chem. Soc.* **2005**, *127*, 5613.
(66) Greczynski, G.; Kugler, T.; Keil, M.; Osikowicz, W.; Fahlman, M.; Salaneck, W. R. *J. Electron Spectrosc. Relat. Phenom.* **2001**, *121*, 1.
(67) Pangborn, A. B.; Giardello, M. A.; Grubbs, R. H.; Rosen, R. K.; Timmers, F. J. *Organometallics* **1996**, *15*, 1518.

(68) Mozer, A. J.; Denk, P.; Scharber, M. C.; Neugebauer, H.; Sariciftci, N. S.; Wagner, P.; Lutsen, L.; Vanderzande, D. *J. Phys. Chem. B* **2004**, *108*, 5235.
(69) Izadyar, A.; Omer, K. M.; Liu, Y.; Chen, S.; Xu, X.; Bard, A. J. *J. Phys. Chem. C* **2008**, *112*, 20027.
(70) Debad, J. D.; Morris, J. C.; Magnus, P.; Bard, A. B. *J. Org. Chem.* **1997**, *62*, 530.
(71) Tonzola, C. J.; Alam, M. M.; Kaminsky, W.; Jenekhe, S. A. *J. Am. Chem. Soc.* **2003**, *125*, 13548.
(72) Kulkarni, A. P.; Tonzola, C. J.; Babel, A.; Jenekhe, S. A. *Chem. Mater.* **2004**, *16*, 4556.
(73) Poriel, C.; Liang, J.-J.; Rault-Berthelot, J.; Barrière, F.; Cocherel, N.; Slawin, A. M. Z.; Horhant, D.; Virboul, M.; Alcaraz, G.; Audebrand, N.; Vignau, L.; Huby, N.; Wantz, G.; Hirsch, L. *Chem.—Eur. J.* **2007**, *13*, 10055.
(74) Shrotriya, V.; Li, G.; Yao, Y.; Moriarty, T.; Emery, K.; Yang, Y. *Adv. Funct. Mater.* **2006**, *16*, 2016.
(75) Curtis, R. F.; Phillips, G. T. *J. Chem. Soc.* **1965**, 5134.
(76) Tour, J. M.; Wu, R. *Macromolecules* **1992**, *25*, 1901.
(77) Irwin, M. D.; Liu, J.; Leever, B. J.; Hersam, M. C.; Durstock, M. F.; Marks, T. J., *Langmuir*, in press.
(78) Kong, J.; White, C. A.; Krylov, A. I.; Sherrill, D.; Adamson, R. D.; Furlani, T. R.; Lee, M. S.; Lee, A. M.; Gwaltney, S. R.; Adams, T. R.; Ochsenfeld, C.; Gilbert, A. T. B.; Kedziora, G. S.; Rassolov, V. A.; Maurice, D. R.; Nair, N.; Shao, Y.; Besley, N. A.; Maslen, P. E.; Dombroski, J. P.; Daschel, H.; Zhang, W.; Korambath, P. P.; Baker, J.; Byrd, E. F. C.; Voorhis, T. V.; Oumi, M.; Hirata, S.; Hsu, C.-P.; Ishikawa, N.; Florian, J.; Warshel, A.; Johnson, B. G.; Gill, P. M. W.; Head-Gordon, M.; Pople, J. A. *J. Comput. Chem.* **2000**, *21*, 1532.
(79) Maldonado, J.-L.; Bishop, M.; Fuentes-Hernandez, C.; Caron, P.; Domercq, B.; Zhang, Y.-D.; Barlow, S.; Thayumanavan, S.; Malagoli, M.; Brédas, J.-L.; Marder, S. R.; Kippelen, B. *Chem. Mater.* **2003**, *15*, 994.
(80) Smeu, M.; Wolkow, R. A.; KiLabio, G. A. *J. Chem. Phys.* **2008**, *129*, 034707.
(81) DiLabio, G. A.; Pratt, D. A.; Wright, J. S. *J. Org. Chem.* **2000**, *65*, 2195.
(82) Rohde, D.; Dunsch, L.; Tabet, A.; Hartmann, H.; Fabian, J. *J. Phys. Chem. B* **2006**, *110*, 8223.
(83) Li, J.; Wang, L.; Liu, J.; Evmenenko, G.; Dutta, P.; Marks, T. J. *Langmuir* **2008**, *24*, 5755.
(84) Huang, Q.; Li, J.; Marks, T. J.; Evmenenko, G. A.; Dutta, P. *J. Appl. Phys.* **2007**, *101*, 093101.
(85) Cui, J.; Huang, Q.; Veinot, J. C. G.; Yan, H.; Wang, Q.; Hutchinson, G. R.; Richter, A. G.; Evmenenko, G.; Dutta, P.; Marks, T. J. *Langmuir* **2002**, *18*, 9958.
(86) Louie, J.; Hartwig, J. F. *Tetrahedron Lett.* **1995**, *36*, 3609.
(87) Guram, A. S.; Rennels, R. A.; Buchwald, S. L. *Angew. Chem., Int. Ed.* **1995**, *34*, 1348.
(88) Driver, M. S.; Hartwig, J. F. *J. Am. Chem. Soc.* **1996**, *118*, 7217.
(89) Wolfe, J. P.; Wagaw, S.; Buchwald, S. L. *J. Am. Chem. Soc.* **1996**, *118*, 7215.
(90) Hartwig, J. F. *Angew. Chem., Int. Ed.* **1998**, *37*, 2046.
(91) Yang, B. H.; Buchwald, S. L. *J. Organomet. Chem.* **1999**, *576*, 125.
(92) Hooper, M. W.; Utsunomiya, M.; Hartwig, J. F. *J. Org. Chem.* **2002**, *68*, 2861.
(93) Huang, Q.; Li, J.; Evmenenko, G. A.; Dutta, P.; Marks, T. J. *Chem. Mater.* **2006**, *18*, 2431.
(94) Bard, A. J.; Faulkner, L. R. *Electrochemical Methods: Fundamentals and Applications*, 2nd ed.; John Wiley & Sons Inc.: New York, 2001.
(95) Chambon, S.; Rivaton, A.; Gardette, J.-L.; Firon, M. *Sol. Energy Mater. Sol. Cells* **2008**, *92*, 785.
(96) Shrotriya, V.; Ouyang, J.; Tseng, R. J.; Li, G.; Yang, Y. *Chem. Phys. Lett.* **2005**, *411*, 138.
(97) Mihailetchi, V. D.; Wildeman, J.; Blom, P. W. M. *Phys. Rev. Lett.* **2005**, *94*, 126602.
(98) Yan, H.; Yoon, M.-H.; Facchetti, A.; Marks, T. J. *Appl. Phys. Lett.* **2005**, *87*, 183501.
(99) We recognize that the charge-transfer directions in OFETs and OPVs are parallel and perpendicular, respectively, to the substrate plane. However, there is no evidence that the film microstructures are in any way anisotropic.
(100) Mihailetchi, V. D.; Blom, P. W. M.; Hummelen, J. C.; Rispens, M. T. *J. Appl. Phys.* **2003**, *94*, 6849.
(101) Aernouts, T.; Geens, W.; Poortmans, J.; Heremans, P.; Borghs, S.; Mertens, R. *Thin Solid Films* **2002**, *403*, 297–404.
(102) Smith, A. P.; Smith, R. R.; Taylor, B. E.; Durstock, M. F. *Chem. Mater.* **2004**, *16*, 4687.
(103) Yang, X.; Loos, J. *Macromolecules* **2007**, *40*, 1353.
(104) van Bavel, S. S.; Sourty, E.; de With, G.; Loos, J. *Nano Lett.* **2009**, *9*, 507.
(105) Mayer, A. C.; Toney, M. F.; Scully, S. R.; Rivnay, J.; Brabec, C. J.; Scharber, M.; Koppe, M.; Heeney, M.; McCulloch, I.; McGehee, M. D. *Adv. Funct. Mater.* **2009**, *19*, 1.
(106) Kim, Y.; Choulis, S. A.; Nelson, J.; Bradley, D. D. C.; Cook, S.; Durrant, J. R. *Appl. Phys. Lett.* **2005**, *86*, 063502.
(107) Bernède, J. C. *J. Chil. Chem. Soc.* **2008**, *53*, 1549.
(108) Vogel, M.; Doka, S.; Breyer, C.; Lux-Steiner, M. C.; Fostiropoulos, K. *Appl. Phys. Lett.* **2006**, *89*, 163501.

AM900634A